

Modulus-mismatch strategy optimized lightweight refractory high-entropy alloys for superior synergy of mechanical properties and thermostability

Bang Dou ^a, Jiaxiang Cui ^a, Rong Guo ^a, Shien Liu ^a, Tianrui Zhang ^a, Songshen Chen ^c, Bolun Li ^d, Xutao Wang ^e, Benpeng Wang ^{a,b}, Shihai Sun ^{a,b}, Liang Wang ^{a,*}, Yunfei Xue ^{a,b,**}

^a School of Materials Science and Engineering, Beijing Institute of Technology, Beijing, 100081, China

^b Tangshan Research Institute, BIT, Tangshan, 063099, China

^c Beijing Aerospace Wairun High Tech Co. Ltd, Beijing, 100081, China

^d Chongqing Hongyu Precision Industry Group Co. Ltd, Bishan, Chongqing, 402760, China

^e Beijing Electro-Mechanical Engineering Institute, Beijing, 100074, China



ARTICLE INFO

Keywords:

Lightweight refractory high-entropy alloys
Shear modulus mismatch
Solid solution strengthening
Strength-ductility balance

ABSTRACT

Lightweight refractory high-entropy alloys (LRHEAs) have received significant attention due to their excellent strength-plasticity matching. Generally, its strengthening mechanism mainly comes from solid solution strengthening caused by atomic radius mismatches, but excessive atomic radius mismatch can reduce the phase stability of solid solution and easily generate precipitated phases to reduce the plasticity. Here, we present a strategy to enhance the shear modulus mismatch while improving the mechanical properties and phase stability of LRHEAs. We chose the TiZrVNbAl system as the LRHEAs model. The addition of Mo resulted in a modulus mismatch induced strength contribution of 564 MPa, which accounts for ~57 % of the total strength. Compared to the alloy without Mo, the strength increased by ~42 % without any loss of ductility. More importantly, the addition of Mo significantly reduces the diffusion coefficient of the main element and realizes the effective kinetic suppression of the precipitated phase. This enables the alloy to avoid brittle precipitate generation even after aging at 500 °C for 5 h, and hence the excellent mechanical properties are well kept. Additionally, the strength of the LRHEA is increased by more than two times at 700 °C, demonstrating higher high temperature performance compared to RHEAs with tensile ductility. Utilizing the shear modulus mismatch strategy can effectively enhance the solid solution strengthening effect, improving the comprehensive mechanical properties of the alloy at room temperature and high temperature, while also improving phase stability. This provides a new approach to developing structurally stable high-performance alloys.

1. Introduction

The mechanical properties and lightness of metal structural materials have always attracted much attention. In recent years, high-entropy alloys (HEAs) with novel properties due to the complex interactions between multiple principal elements have received wide attention in the field of materials [1–3]. Based on this, lightweight refractory HEAs (LRHEAs) comprising refractory metals (Ti, Zr, V, Nb, etc.) and lightweight metals (Al, Mg, etc.) have surfaced [4–6]. These alloys display high strength due to remarkable solid solution strengthening, and are also highly ductile owing to the relatively low valence electron concentration [7,8].

Currently, most LRHEAs use atomic size mismatch to provide a solid solution strengthening effect to achieve high strength [9,10]. For example, solid solution strengthening contributes 60 % of the total strength in TiZrHfNb and TiZrVNbAl alloys [11,12]. However, large atomic size mismatches can lead to the formation of brittle precipitate phases and reduce ductility [13,14]. This phenomenon of brittle precipitation deteriorating plasticity is exacerbated in the preparation of large-size ingots. This is due to the air-cooling process of large-size ingots after heat treatment, which often requires several hours of holding in the temperature range of 400–600 °C. However, a large number of LRHEAs reported so far are prone to produce brittle phases and deteriorate ductility after being held at 400–600 °C for several hours [15,16],

* Corresponding author.

** Corresponding author. School of Materials Science and Engineering, Beijing Institute of Technology, Beijing, 100081, China.

E-mail addresses: lwangbit@bit.edu.cn (L. Wang), xueyunfei@bit.edu.cn (Y. Xue).

Table 1

Shear modulus (G) and atomic radius (r) of Ti, Zr, V, Nb, Al, Mo elements [8].

	Ti	Zr	V	Nb	Al	Mo
G (GPa)	44	33	47	38	26	125.6
r (pm)	142.5	156.3	132.9	142.9	135.9	136.3

thus affecting their engineering applications.

By analyzing the multicomponent solid-solution strengthening model developed by Toda-Caraballo [17,18], it has been discovered that the shear modulus mismatch plays a significant role in solid solution strengthening, in addition to the previously mentioned atomic radius mismatch. Nonetheless, the contribution of the shear modulus mismatch to strengthening is generally relatively small. Hence, the researchers in the past have designed alloys based on solid solution strengthening mainly from an atomic radius mismatch perspective, with relatively little consideration of shear modulus mismatch [19,20]. The emergence of the concept of multi-component effect design for HEAs, which allows for greater solid solubility of high-modulus elements, may promote greater advantages of shear modulus mismatch in solid solution strengthening and provide a new path for the development of high-performance alloys.

Therefore, we chose the non-equiautomic TiZrVNbAl LRHEA with excellent tensile ductility as the research model, and added the high-modulus Mo element (Mo = 0, 7 at%, named M0 and M7) to seek the shear modulus mismatch to play a greater solid solution strengthening effect, while improving the stability of the alloy. Shear modulus and atomic radius for these elements are shown in Table 1. The study demonstrates that the addition of high modulus Mo elements increased the strength by ~42 % while maintaining good ductility. The addition of Mo also increased the phase stability of LRHEAs at 500 °C. In addition, we investigated the high-temperature properties, as well as analyzed the phase stability and solid solution strengthening mechanisms.

2. Experimental

The M0 and M7 LRHEAs ingots were prepared by vacuum suspension melting furnace in argon atmosphere using high-purity (99.95 wt%) Ti, Zr, V, Nb, Al and Mo. Before melting, the metal monomers were mechanically polished and ultrasonically cleaned to remove oxide skin and other impurities on their surfaces. The ingots were repeatedly melted four times to ensure a uniform composition. Afterward, all the ingots were sealed in a quartz tube filled with argon, and homogenized at 1150 °C for 2 h followed by water quenching. Then, to address the issue of large ingots spending more time in the 400–600 °C temperature range due to slower cooling rates and resulting precipitated phases, we conducted an aging treatment with a 5-h hold at 500 °C to study the effect of

Mo on the phase stability of the alloy in the mid-temperature range. The density of the LRHEAs was determined using Archimedes principle.

Dog-bone tensile samples ($1 \times 3 \times 10 \text{ mm}^3$) of the homogenized and aged samples were machined using wire cut electrical discharge machining, and three samples were prepared for each condition to verify repeatability. Tensile tests were conducted at room temperature using a universal testing machine (CMT4105) with a strain rate of 10^{-3} s^{-1} . And cylinders of $\Phi 8 \times 12 \text{ mm}^3$ were prepared in the homogenized samples, and then high-temperature compression tests with a strain rate of 10^{-3} s^{-1} were performed on a Gleeble 3500 thermal simulator.

The phase structure was analyzed by X-ray (D8 Advance, Bruker AXS, Germany) technique with a scanning rate of $5^\circ/\text{min}$ and scanning angles of $20\text{--}100^\circ$. The microstructure of the alloys was observed using a scanning electron microscope (SEM, Regulus8230, Hitachi, Japan) equipped with an energy dispersive spectrometer (EDS) detector and electron backscatter diffraction (EBSD). The phase structure and elemental composition of the precipitated phase were studied by transmission electron microscope (TEM) with energy dispersive spectroscopy (EDS).

3. Results

3.1. Microstructural investigation

To analyze the effect of Mo element on the phase structure and microstructure of LRHEAs, the homogenized M0 and M7 alloys were characterized by X-ray diffraction (XRD), back scattered electron (BSE) and EDS, the results are shown in Fig. 1. From Fig. 1(a), it is seen that the homogenized M0 and M7 alloys contain only body-centered cubic (BCC) diffraction peaks, indicating that both LRHEAs exhibited a single BCC structure. The densities of M0 and M7 alloys are 5.59 g/cm^3 and 5.87 g/cm^3 , respectively. Fig. 1(b and c) indicate that the distribution of elements is uniform and the grain sizes of the M0 and M7 alloys are $\sim 364 \mu\text{m}$ and $\sim 345 \mu\text{m}$, respectively.

Phase stability is a crucial factor in preparing large-size ingots to ensure stable components in practical production. Good phase stability of the alloy in the mid-temperature range is especially important for this purpose. Therefore, we processed aged treatment on LRHEAs at 500 °C, and the microstructure was analyzed by BSE and TEM techniques, as shown in Fig. 2. The M0 alloys exhibit a multi-phase structure, with the occurrence of a bright white precipitated phase at the grain boundaries, as indicated by yellow circles in Fig. 2(a). In contrast, the M7 alloys manifest a single-phase structure without any visible precipitates at the grain boundaries, as demonstrated in Fig. 2(b). The composition and structure of the precipitated phase in M0 alloy was analyzed, with corresponding results reported in Fig. 2(c). SAED and EDS results indicated

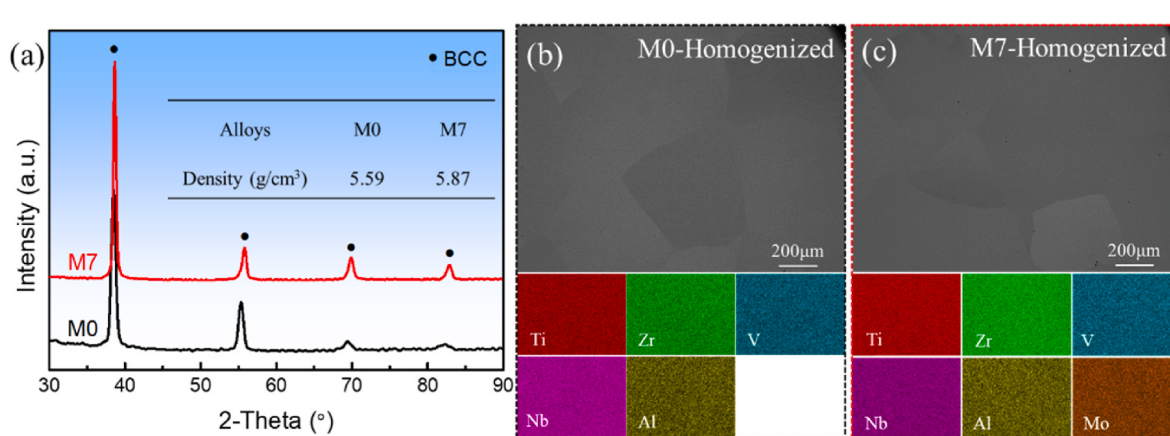


Fig. 1. (a) XRD patterns and density of the homogenized M0 and M7 LRHEAs; BSE images and EDS elemental maps: (b) homogenized M0 alloys, (c) homogenized M7 alloys.

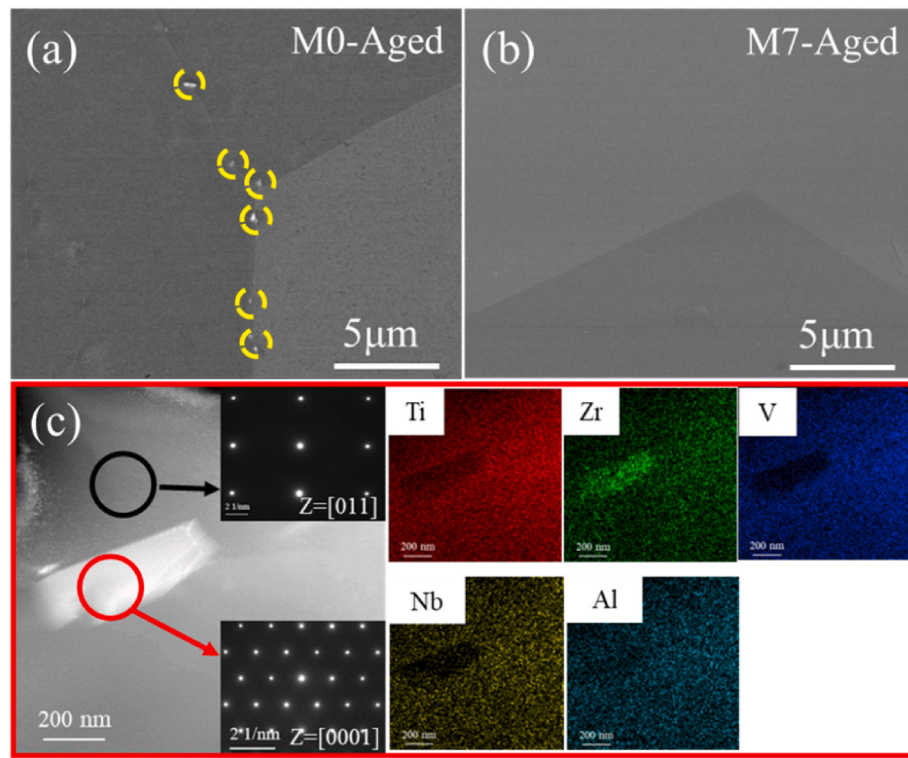


Fig. 2. (a, b) BSE images of the aged M0 and M7 LRHEAs; (c) SAED image and EDS elemental maps of precipitated phase.

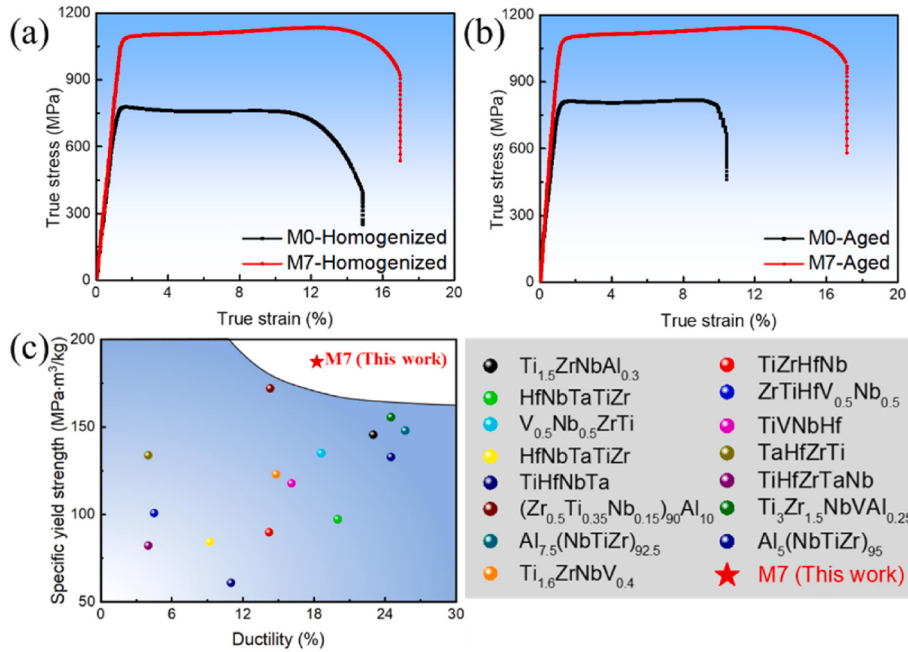


Fig. 3. Tensile stress-strain curves of the (a) homogenized and (b) aged LRHEAs obtained at room temperature; (c) Specific yield strength and fracture ductility of M7 alloy compared to other representative RHEAs.

Table 2
Yield strength ($\sigma_{0.2}$) and ductility (ε) of M0 and M7 alloys.

Alloys	Homogenized		Aged	
	$\sigma_{0.2}$ (MPa)	ε (%)	$\sigma_{0.2}$ (MPa)	ε (%)
M0	760 ± 13	15 ± 2	774 ± 12	11 ± 3
M7	1079 ± 16	17 ± 3	1080 ± 14	17 ± 2

that the bright white precipitated phase is rich in Zr with a hexagonal close-packed (HCP) structure. The addition of Mo element to LRHEAs can hinder the formation of Zr-rich precipitates, thus enhancing the phase stability of LRHEAs at intermediate temperature.

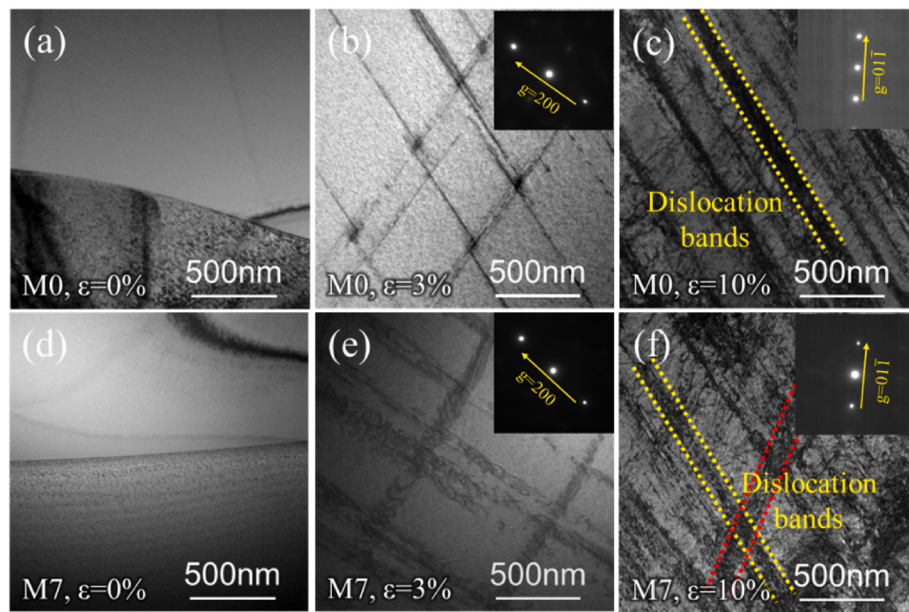


Fig. 4. Deformed microstructure of homogenized M0 and M7 alloys observed by TEM; (a, d) Undeformed structure, (b, e) ~3 % deformation structure, (c, f) ~10 % deformation structure.

3.2. Mechanical behavior at room temperature

3.2.1. Tensile properties

To validate the impact of Mo element on the strength and ductility of LRHEAs, we conducted tensile tests at room temperature on homogenized and aged samples of M0 and M7 alloys, the results are shown in Fig. 3(a and b). The relevant values of LRHEAs obtained during tensile tests are summarized in Table 2. From the stress-strain curves of the homogenized samples in Fig. 3(a), it can be seen that the addition of Mo element to LRHEAs enhances the strength and ductility. When the Mo content is raised from 0 to 7 %, the strength of the alloy increases from ~760 MPa to ~1079 MPa, resulting in a strength enhancement of ~42

%, showing excellent solid solution strengthening effect. Additionally, the ductility increases from ~15 % to ~18 %, indicating that the solid solution strengthening introduced by Mo did not result in any loss of plastic deformation. The stress-strain curves of the aged samples in Fig. 3(b) demonstrated that the yield strengths of the two LRHEAs after aging are similar to those of homogenized ones. Nevertheless, the fracture ductility of the M0 alloys diminished considerably to ~11 %, while the ductility of the M7 alloys remained almost unchanged. The above results suggest that the formation of Zr-rich phases leads to a reduction in the ductility of the alloys. In addition, the results support the notion that the addition of Mo element can prevent the development of brittle phases and improve the phase stability of LRHEAs at intermediate

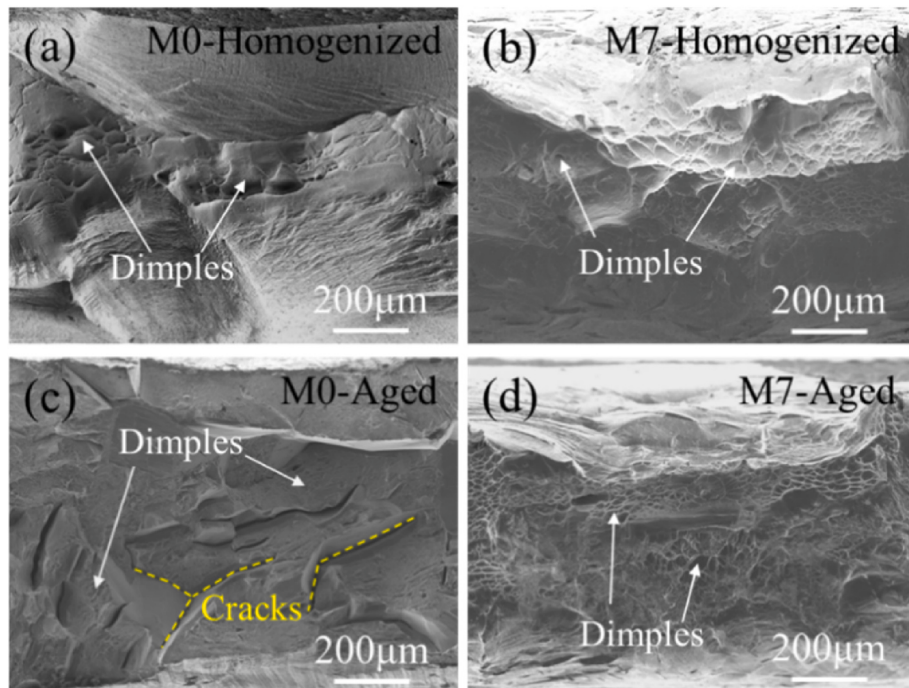


Fig. 5. Tensile fracture morphologies of M0 and M7 LRHEAs.

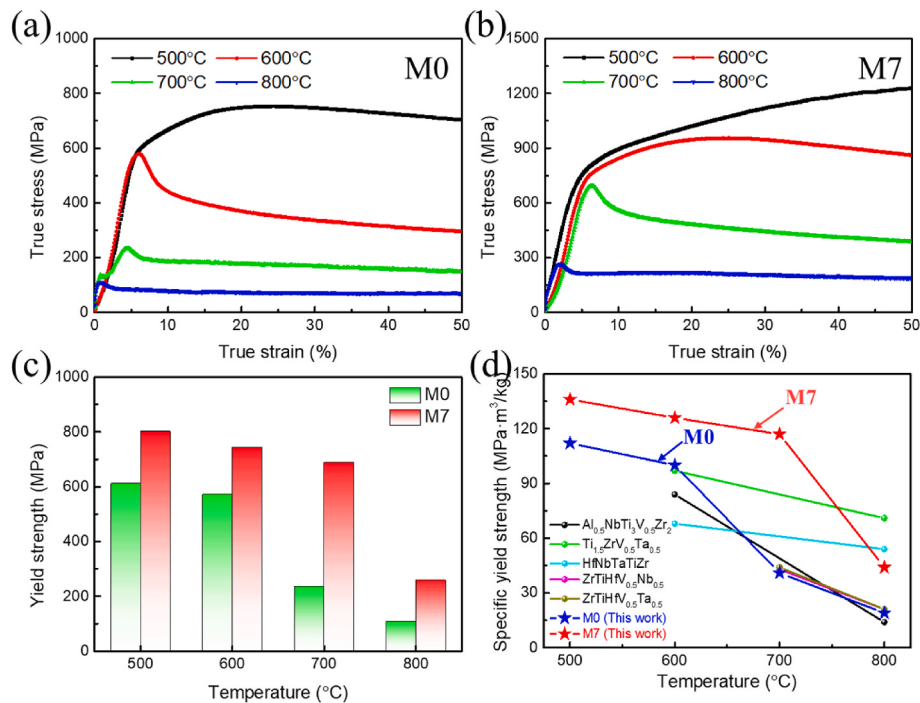


Fig. 6. Compression stress-strain curves obtained during the testing of (a) M0 and (b) M7 LRHEAs; (c) Yield strength of M0 and M7 LRHEAs in the range of 600–800 °C; (d) Specific yield strength as a function of testing temperature of M7 LRHEA in comparison with other representative alloys.

temperatures.

The specific yield strength and fracture ductility of the M7 LRHEA was compared to other representative RHEAs (Fig. 3(c)) [21–34]. Among the surveyed, M7 LRHEA has a higher specific yield strength and excellent fracture ductility. Additionally, M7 alloys demonstrate significant mechanical property advantages at room temperature over other RHEAs.

3.2.2. Microstructure evolution

The TEM technique was used to investigate the dislocation behavior of homogenized M0 and M7 LRHEAs under different strains to reveal the deformation behavior. Fig. 4(a–d) displays the undeformed M0 and M7 alloy, which verify that they are all single-phase BCC structures with no dislocation lines present. Low-strain (~3 %) samples in Fig. 4(b)(e) demonstrate a cross-slip system parallel to each other, indicating that multiple slip systems were activated simultaneously in both M0 and M7 alloys at the early stage of deformation. As the sample deformation increases to ~10 % strain, the high-density dislocation wall is formed by dislocation cross slip, which effectively promotes the durability of plastic deformation [35].

The study examined the tensile fracture morphology of homogenized and aged M0 and M7 LRHEAs, as presented in Fig. 5, to identify the cause of the decrease ductility in aged M0 sample. Results from Fig. 5(a and b) demonstrated that homogenized M0 and M7 alloys are mainly covered by dimples and plastic tear ridges, performing a typical ductile fracture pattern that gives the alloys excellent ductility. In contrast, the aged M0 sample exhibit a significant number of cracks distributed along the grain boundaries (yellow dashed line in Fig. 5(c)) in addition to the ductile dimples. This indicate that the fracture mechanism of the aged M0 sample consists of ductile fracture and brittle fracture along the grain. The generation of a Zr-rich phase (Fig. 2(a)) weakening the grain boundaries at the aged M0 alloys, which preferentially forms crack sources and extends along the grain boundaries [36,37]. From Fig. 5(d), it can be seen that the aged M7 sample still shows ductile fracture. Therefore, the addition of Mo element to LRHEAs can inhibit the generation of brittle Zr-rich phase and maintain the high ductility.

3.3. Mechanical behavior at high temperature

3.3.1. Compressive properties

Under the premise of ensuring good strong plasticity at room temperature, improving the high-temperature mechanical properties of the alloy is the key to expanding its applications. Based on the results of phase stability and mechanical properties in 3.1 and 3.2, we analyzed that the alloy may have excellent high-temperature properties. For this reason, we conducted high-temperature compression experiments on M0 and M7 LRHEAs in the range of 500–800 °C. The true stress-strain curves obtained from high-temperature uniaxial compression tests are shown in Fig. 6(a and b), and the high-temperature yield strengths ($\sigma_{0.2}$) of the two LRHEAs were plotted on a histogram (Fig. 6(c)). At 500 °C and 600 °C, the yield strength of M7 alloy was approximately 200 MPa higher than that of M0 alloy. When the temperature was increased to 700 °C and 800 °C, the yield strength of M7 alloy was more than two times higher than that of M0 alloy, indicating that the addition of Mo to LRHEAs can maintain the solid solution strength effect up to higher temperatures. Additionally, it was observed that, like most LRHEAs, the yield strength of M0 and M7 alloys gradually decreases with increasing temperature [38–40].

As can be seen in Fig. 6(a), M0 LRHEA initially exhibit strain-hardening phenomenon in the 500 °C test and show strain-softening after reaching the peak value. When the temperature rises to 600–800 °C, M0 alloys demonstrate a softening behavior immediately after reaching the yield strength. During the deformation of M7 alloy at 500 °C, the plastic phase always exhibits strain hardening. At 600 °C, the early stage of plastic deformation also shows obvious strain hardening, when the temperature reaches 700 °C or higher, the deformation will immediately manifest as strain softening upon reaching the yield point. Comparison of the two alloys of the plastic deformation stage, add Mo can significantly improve the strain hardening to the strain softening of the critical temperature of the transition.

In addition, the temperature dependence of the specific yield strength of M0 and M7 LRHEAs was evaluated and compared to other representative RHEAs with room temperature tensile plasticity (Fig. 6(d)) [33,41,42]. The specific yield strengths of M7 LRHEAs were

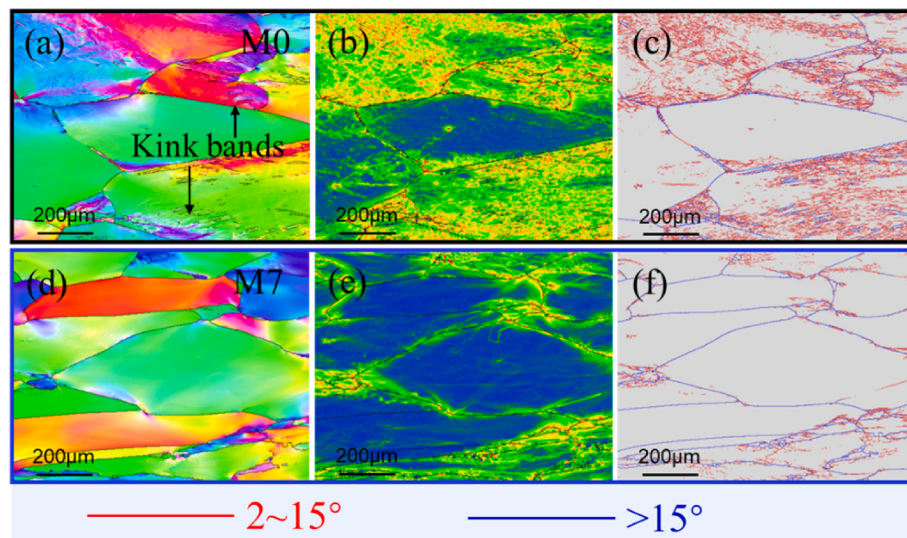


Fig. 7. Microstructures of LRHEAs after a compressive strain, $\varepsilon \sim 50\%$ deformed at $600\text{ }^\circ\text{C}$; (a, d) EBSD-IPF maps, (b, e) local misorientation maps and (c, f) grain boundaries of M0 and M7 alloys.

substantially higher than those of M0 LRHEAs in the range of $500\text{ }^\circ\text{C}$ - $700\text{ }^\circ\text{C}$. Compared to other RHEAs with tensile ductility, M7 LRHEAs demonstrate significant mechanical property advantages in the $500\text{ }^\circ\text{C}$ - $700\text{ }^\circ\text{C}$ range.

3.3.2. Microstructure evolution

In order to investigate the effect of Mo content on the strength and strain hardening mechanism during high-temperature deformation, two samples of LRHEAs deformed in compression at $600\text{ }^\circ\text{C}$ were analyzed by EBSD. The results are displayed in Fig. 7, revealing that multiple deformation bands are visible in a few initial grains of M0 alloy, as shown in Fig. 7(a). This suggests that kink bands are formed in the M0 alloy during deformation at $600\text{ }^\circ\text{C}$ [43]. This means that the M0 alloys undergo severe localized plastic deformation during deformation at $600\text{ }^\circ\text{C}$, which is most visually manifested by the occurrence of stress softening [44]. As can be seen from Fig. 7(d), M7 alloy have relatively uniform deformation degrees, so there is strain hardening in the deformation process (Fig. 6(b)). The resistance to dislocation motion is increased by the addition of Mo to the LRHEAs phase, which in turn retards the formation of kink bands.

Fig. 7(b, c, e, f) displays the grain boundary reconfiguration and local misorientation maps of LRHEAs, and the volume fraction (approximate area fraction) of small-angle grain boundaries of M0, M7 alloys are $\sim 68\%$ and $\sim 17\%$, respectively. Which indicate that the addition of Mo element in LRHEAs reduces the occurrence of dynamic recovery (DRV) during the deformation process at $600\text{ }^\circ\text{C}$. As is commonly, the formation of DRV is usually accompanied by the mutual cancellation of dislocation motion and dislocation rearrangement, indicating that the alloy is more susceptible to plastic deformation resulting in decreased strength. Therefore, adding Mo to LRHEAs limits atomic diffusion, which reduces the processes of dislocation nucleation and climbing, and inhibiting DRV behavior to maintain high strength of the alloy [45].

4. Discussion

The results above demonstrate that the addition of Mo elements to LRHEAs has effectively led to a simultaneous enhancement strength and fracture ductility in room temperature, as well as an improvement in phase stability and high temperature properties of the alloys. In this study, we focus on analyzing the reasons for both improved phase stability and mechanical properties resulting from Mo element incorporation.

Table 3

Melting point (K) and yield strength (σ_{YS}) of Ti, Zr, V, Nb, Al elements [11,12].

Elements	Ti	Zr	V	Nb	Al	Mo
T (K)	1941	2128	2183	2750	933	2896
σ_{YS} (MPa)	195	280	103	240	276	420

4.1. Effect of Mo element on phase stability of LRHEAs

From Fig. 2, it is clear that the inclusion of Mo in LRHEAs inhibits Zr-rich phase formation. To comprehend the impact of Mo on phase stability, we will explore the thermodynamic and kinetic aspects separately. First, we analyze the effect of Mo element on the phase stability by thermodynamics. Several thermodynamic parameters have been used to help understand the phase stability of HEAs, among which, Ω and δ are important parameters for determining the phase stability. Zhang et al. [46] concluded that higher values of Ω are indicative of stronger high entropy effects, resulting in more stable solid solutions. Meanwhile, Liu et al. [47] argued that lowering δ would attenuate the distortion energy of the alloy, which in turn improves the phase stability. These two parameters can be calculated using the following formula [46].

$$\Omega = \frac{T_m \Delta S_{mix}}{|\Delta H_{mix}|} \quad (1)$$

$$\Delta S_{mix} = -R \sum_{i=1}^n c_i \ln c_i \quad (2)$$

$$\Delta H_{mix} = 4 \sum_{i=1, i \neq j}^n \Delta H_{ij} c_i c_j \quad (3)$$

$$\delta = \sqrt{\sum_{i=1}^n c_i \left(1 - \frac{r_i}{\bar{r}}\right)^2} \quad (4)$$

Here, $T_m = \sum_{i=1}^n c_i T_i$ is the average melting temperature of the alloy, and T_i is the melting point of the i th element; c_i and c_j are the mole fractions of the i th and j th elements; R is the gas constant; ΔH_{ij} is the mixing enthalpy of binary liquid alloys [48]; r_i is the atomic radius of the i th element (In Table 1); $\bar{r} = \sum_{i=1}^n c_i r_i$ is the average atomic radius of the alloy. The values of T for Ti, Zr, V, Nb, Al, Mo elements are listed in Table 3. The Ω and δ values of M0 and M7 LRHEAs were calculated

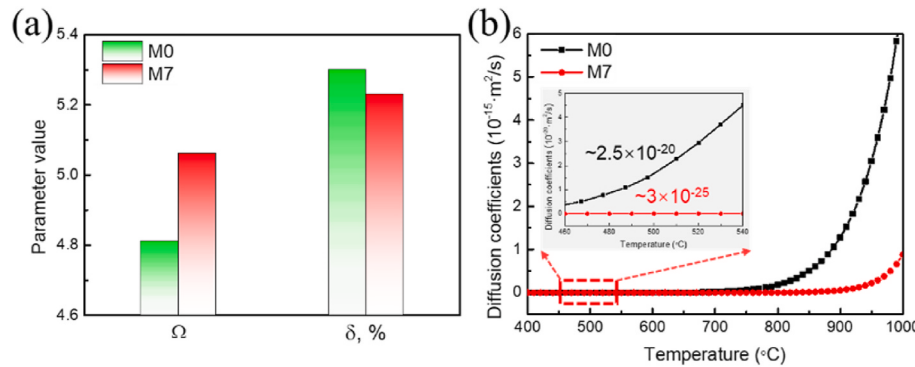


Fig. 8. (a) The calculated Ω and δ of the LRHEAs; (b) Diffusion coefficient of Zr in solid solution.

according to Eqs. (1)–(4), and the results are shown in Fig. 8(a). The M7 alloy has a notably higher Ω value compared to the M0 alloy, and also a smaller δ value. This implies that the addition of Mo element in LRHEAs not only enhances the high entropy effect, but also reduces the distortion energy, thus rendering the alloy more stable.

Next, we analyzed the effect of Mo elements on the phase transition rate of LRHEAs through kinetics. The diffusion coefficient of Zr in solid solution was calculated using the equilibrium calculator module of the CALPHAD software, with selected thermodynamic, property and mobility databases of HEAs [49,50], as shown in Fig. 8(b). At the same temperature, the diffusion coefficient of Zr in solid solution becomes smaller with the increase of Mo content, indicating that the increase of Mo content in LRHEAs effectively reduces the atomic diffusion rate. In particular, the diffusion coefficients have a huge difference in the intermediate temperature range of 460 $^\circ\text{C}$ –540 $^\circ\text{C}$, the diffusion coefficients of Zr in M0 alloys are about ten thousand times higher than in M7 alloys, as shown in the inset of Fig. 8(b), which means that the increase of Mo content greatly improves the stability of LRHEAs solid solution. This is consistent with the results in this paper for M0 and M7 alloys aged at 500 $^\circ\text{C}$. As shown in Fig. 2, the M0 alloy precipitates the Zr-rich phase, while the M7 alloy remains a single-phase BCC structure. The inclusion of Mo in LRHEAs can significantly decrease the diffusion coefficient of atoms in the system and enhance the stability of the alloy phase.

4.2. Strengthening mechanism

The aim of this study is to achieve strength enhancement by using the shear modulus mismatch gain solid solution strengthening effect, here we systematically analyzed the changes in strength before and after Mo was added using a solid solution strengthening model, to determine the strengthening effect of Mo, and to analyze the shear modulus mismatch strengthening effect and the atomic radius mismatch effect of the two alloys. Assessment of the contribution to strength enhancement resulting from the modulus strengthening introduced by Mo. For single-phase alloys, solution strengthening (SSS) and grain boundary strengthening are the main strengthening mechanisms. It can be seen from Fig. 1 that the LRHEAs in this work are single-phase structures, and the grain sizes of all the alloys exceed 200 μm . Therefore, solid solution strengthening is the main strengthening mechanism of LRHEAs, since the effect of grain boundary strengthening is small and can be ignored [51,52].

According to the classical solid solution strengthening theory, the distorted elastic field caused by the introduction of solute atoms impedes dislocation motion. Xu Jian et al. [53] developed a computational model utilizing classical solid solution theory for BCC-HEAs. This model estimates the yield strength (σ_{YS}) using the following equation:

$$\sigma_{YS} = \sigma_{YS}^{ROM} + \Delta\sigma_{ss} \quad (5)$$

Where σ_{YS}^{ROM} is the yield stress obtained by the rule of mixtures, which is

Table 4

Contribution of different strengthening mechanisms to the yield strength of LRHEAs.

Alloys	σ_{YS}^{ROM} (Mpa)	$\Delta\sigma_{ss}$ (Mpa)
M0	209	460
M7	223	760

estimated as $\sigma_{YS}^{ROM} = \sum c_i \sigma_{YS}^i$, and c_i and σ_{YS}^i (In Table 3) are the mole fraction and yield stress of each constituent element i , respectively. $\Delta\sigma_{ss}$ represents the contribution of SSS to yield strength, which can be described as:

$$\Delta\sigma_{ss} = G \left(\sum f_i^2 c_i \right)^{2/3} / 45 \quad (6)$$

Here, $G = \sum G_i c_i$ is the shear modulus of the alloy, G_i is the shear modulus from the i th component (In Table 1). f_i is composed of the atomic radius mismatch (δ_r) and shear modulus misfit (δ_G), which can be calculated as:

$$f_i = \sqrt{\alpha^2 \delta_r^2 + \delta_G^2} \quad (7)$$

Here, α is a dimensionless constant with respect to dislocation categories, and it is designated as 9 in a randomly mixed system containing both edge and screw dislocation [54,55]. σ_{ri} and σ_{Gi} are the average difference between atomic size and atomic modulus, respectively.

$$\delta_{ri} = \frac{9}{8} \sum c_j \delta_{rij} \quad (8)$$

$$\delta_{Gi} = \frac{9}{8} \sum c_j \delta_{Gij} \quad (9)$$

Here, δ_{rij} and δ_{Gij} are the misfits of atomic sizes and shear modulus, respectively. Which can be expressed as:

$$\delta_{rij} = 2 \frac{r_i - r_j}{r_i + r_j} \quad (10)$$

$$\delta_{Gij} = 2 \frac{G_i - G_j}{G_i + G_j} \quad (11)$$

Here, r_i and G_i are the atomic size and shear modulus of the i th component (In Table 1).

The yield strength values of M0 and M7 alloys and the contribution of each strengthening strategy were calculated according to Eqs. 5–11, the results are shown in Table 4 and plotted in Fig. 9. From Fig. 9(a), the calculated and experimental yield strengths for the M0 and M7 alloys show a strong correlation, indicating that the results of the model are plausible. Meanwhile, comparing the σ_{YS}^{ROM} of M7 and M0 alloys, it is

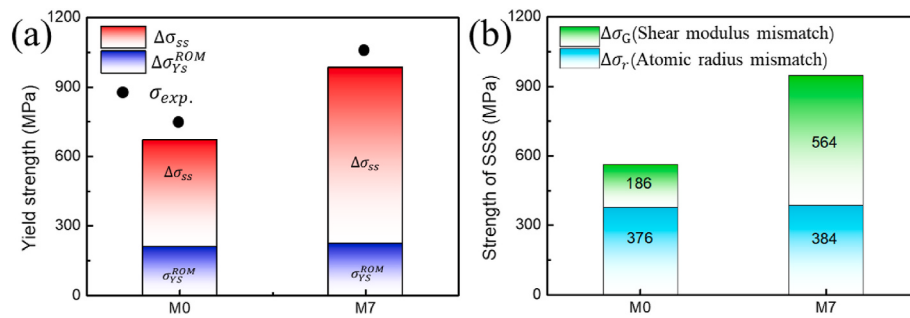


Fig. 9. (a) Contribution of different strengthening mechanisms to yield strength; (b) Strengthening effect induced by atomic radius mismatch ($\Delta\sigma_r$) and modulus mismatch ($\Delta\sigma_G$) for M0 and M7.

Table 5
The contribution of $\Delta\sigma_G$ and $\Delta\sigma_r$ to strength.

Alloys	$\Delta\sigma_G$ (Mpa)	$\Delta\sigma_r$ (Mpa)
M0	376	186
M7	564	384

found to be ~ 210 MPa, which indicates that the addition of Mo does not improve the strength of the alloys from the inherent strength. However, the $\Delta\sigma_{ss}$ value of M07 is higher than that of M0, and the solid solution strengthening effect obviously improves the strength of the alloys by ~ 300 MPa. In order to clarify whether it is the atomic radius mismatch mechanism or the shear modulus mismatch mechanism that is utilized by Mo elements to increase the solid solution strengthening effect. We set $\Delta\delta_{ri}$ or $\Delta\delta_{Gi}$ to 0 and evaluate the strengthening effect of the remaining term in isolation (either the atomic radius related term $\Delta\delta_{ri}$ or the elastic modulus related term $\Delta\delta_{Gi}$). After calculation, the values obtained by M0 were $\Delta\sigma_{ri} = 376$ and $\Delta\sigma_{Gi} = 186$, $\Delta\sigma_{ri} + \Delta\sigma_{Gi} = 562$; the values obtained by M7 were $\Delta\sigma_{ri} = 384$ and $\Delta\sigma_{Gi} = 564$, $\Delta\sigma_{ri} + \Delta\sigma_{Gi} = 948$ (In Table 5), which were similar to the results of solid solution strengthening calculated in Fig. 9(a). The calculated results are plotted in Fig. 9(b), it is clearly seen that the strengthening effects of M0 and M7 alloys relying on atomic mismatches are similar, whereas the strengthening effect of M7 alloy relying on shear modulus mismatch is more than three times that of M0 alloy. The shear modulus mismatch of the M0 alloy provides only ~ 180 MPa of strength, which accounts for $\sim 26\%$ of the total strength. In contrast, the shear modulus mismatch of the M7 alloy provides ~ 564 MPa of strength, which accounts for $\sim 57\%$ of the total strength. Therefore, the increase in yield strength with the addition of Mo element in LRHEAs is mainly dominated by the solid solution strengthening caused by shear modulus mismatch.

To reaffirm the contribution of each element to the atomic and modal mismatches, and to exhibit the distinctiveness of Mo elements to the modal mismatches, we generated line plots for normalized δ_{ri} and δ_{Gi} values of each element. δ_{rAl} has the highest value in M0 and M7 alloys

(Fig. 10(a)), indicating that Al contributes the most to atomic radius mismatch compared to other elements due to the smallest atomic radius of Al atoms. The addition of Mo atoms does not significantly contribute to atomic radius mismatch, therefore providing further evidence that solid solution strengthening of LRHEAs with added Mo elements is not achieved through atomic adaptation. The results of Fig. 10(b) that the δ_{GMo} values are significantly higher than those of other elements in LRHEAs, demonstrating that Mo is the primary contributor to shear modulus mismatch in LRHEAs. This is mainly due to the fact that the high shear modulus of Mo (125.6 GPa) is almost three times higher than that of the other five elements, which triggers a large amount of shear modulus mismatch and the resulting strong solid solution strengthening effect to increase strength.

5. Conclusion

In this paper, the effect of solid solution strengthening induced by shear modulus mismatch on mechanical properties and phase stability is investigated by adding Mo to non-equiautomatic LRHEAs. The strengthening effect of the shear modulus mismatch was increased from 186 MPa to 564 MPa by the addition of Mo, which accounted for $\sim 57\%$ of the total strength. This leads to a $\sim 42\%$ increase in the yield strength of the alloy without any loss of plasticity. The introduction of Mo increases the phase stability of LRHEAs, as demonstrated by 5 h aging treatment at 500 °C. This is because Mo reduces the diffusion coefficient of the main element in the solid solution of LRHEAs, which is effective in inhibiting the formation of precipitated phases. Additionally, the addition of Mo also substantially increases the high-temperature mechanical properties, particularly at 700 °C, where the yield strength more than doubles, realizing excellent mechanical properties over a wide temperature range. This approach of utilizing modulus mismatch to design high-strength, high-plasticity and high-stability matched LRHEAs offers an efficient means of developing new high-performance alloys.

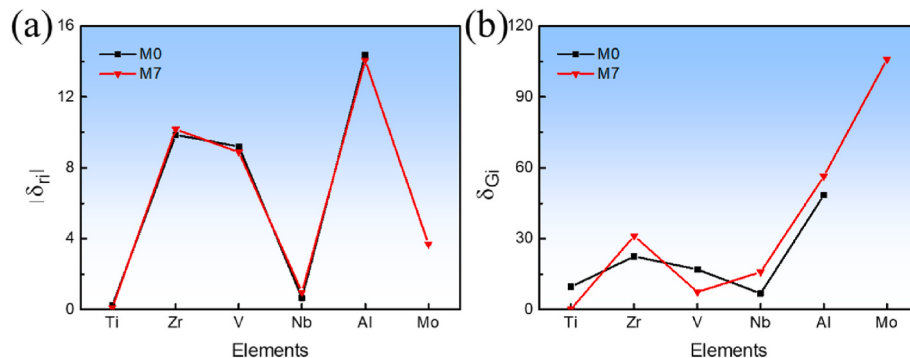


Fig. 10. Normalized (a) δ_{ri} and (b) δ_{Gi} from each element of the LRHEAs.

CRediT authorship contribution statement

Bang Dou: Writing – original draft, Methodology, Investigation, Formal analysis, Data curation. **Jiaxiang Cui:** Investigation, Data curation. **Rong Guo:** Investigation, Data curation. **Shien Liu:** Writing – original draft, Investigation, Data curation. **Tianrui Zhang:** Methodology, Data curation. **Songshen Chen:** Investigation, Data curation. **Bolum Li:** Methodology, Investigation, Data curation. **Xutao Wang:** Methodology, Investigation, Data curation. **Benpeng Wang:** Writing – original draft, Methodology, Investigation, Data curation. **Shihai Sun:** Writing – review & editing, Methodology, Investigation. **Liang Wang:** Writing – review & editing, Formal analysis, Data curation. **Yunfei Xue:** Writing – review & editing, Project administration, Funding acquisition.

Declaration of competing interest

The authors declare that they have no known competing financial interests or personal relationships that could have appeared to influence the work reported in this paper.

Data availability

No data was used for the research described in the article.

Acknowledgments

This work was supported by the National Natural Science Foundation of China (grant number: U2241234, 52301127, and 52171028), and the Scientific Research Foundation for the Youth Scholars of Beijing Institute of Technology (grant number XSQD-2020008003).

References

- [1] J.W. Yeh, S.K. Chen, S.J. Lin, J.Y. Gan, T.S. Chin, T.T. Shun, C.H. Tsau, S.Y. Chang, Nanostructured high-entropy alloys with multiple principal elements: novel alloy design concepts and outcomes, *Adv. Eng. Mater.* 6 (2004) 299–303.
- [2] M. Chuang, M. Tsai, W. Wang, S. Lin, J. Yeh, Microstructure and wear behavior of $\text{Al}_x\text{Co}_{1.5}\text{CrFeNi}_{1.5}\text{Ti}_y$ high-entropy alloys, *Acta Mater.* 59 (2011) 6308–6317.
- [3] S.S. Nene, M. Frank, K. Liu, R.S. Mishra, B.A. McWilliams, K.C. Cho, Extremely high strength and work hardening ability in a metastable high entropy alloy, *Sci. Rep.* 8 (2018) 9920.
- [4] S. Wei, S.J. Kim, J. Kang, Y. Zhang, Y. Yang, T. Furuhara, E.S. Park, C.C. Tasan, Natural-mixing guided design of refractory high-entropy alloys with as-cast tensile ductility, *Nature* 19 (2020) 1175–1181.
- [5] P. Kumar, S.J. Kim, Q. Yu, J. Ell, M. Zhang, Y. Yang, J.Y. Kim, H. Park, A.M. Minor, E.S. Park, R.O. Ritchie, Compressive vs. tensile yield and fracture toughness behavior of a body-centered cubic refractory high-entropy superalloy $\text{Al}_{0.5}\text{Nb}_{1.25}\text{Ta}_{1.25}\text{TiZr}$ at temperatures from ambient to 1200°C, *Acta Mater.* 245 (2023) 118620.
- [6] C. Liu, C. Gadelmeier, S. Lu, J. Yeh, H. Yen, S. Gorsse, U. Glatzel, A. Yeh, Tensile creep behavior of HfNbTaTiZr refractory high entropy alloy at elevated temperatures, *Acta Mater.* 237 (2022) 118188.
- [7] J. Wang, S. Bai, Y. Tang, S. Li, X. Liu, J. Jia, Y. Ye, L.A. Zhu, Effect of the valence electron concentration on the yield strength of Ti–Zr–Nb–V high-entropy alloys, *J. Alloys Compd.* 868 (2021) 159190.
- [8] L. Wang, J. Ding, S. Chen, K. Jin, Q. Zhang, J. Cui, B. Wang, B. Chen, T. Li, Y. Ren, S. Zheng, K. Ming, W. Lu, J. Hou, G. Sha, J. Liang, L. Wang, Y. Xue, E. Ma, Tailoring planar slip to achieve pure metal-like ductility in body-centred-cubic multi-principal element alloys, *Nat. Mater.* 22 (2023) 950–957.
- [9] P. Thirathipiwat, S. Sato, G. Song, J. Bednarcik, K. Nielisch, J. Jung, J. Han, A role of atomic size misfit in lattice distortion and solid solution strengthening of TiNbHfTaZr high entropy alloy system, *Scripta Mater.* 210 (2022) 114470.
- [10] F.G. Courty, M. Kaufman, A.J. Clarke, Solid-solution strengthening in refractory high entropy alloys, *Acta Mater.* 175 (2019) 66–81.
- [11] T. Li, S. Wang, W. Fan, Y. Lu, T. Wang, T. Li, P.K. Liaw, CALPHAD-aided design for superior thermal stability and mechanical behavior in a TiZrHfNb refractory high-entropy alloy, *Acta Mater.* 246 (2023) 118728.
- [12] O.N. Senkov, J.M. Scott, S.V. Senkova, D.B. Miracle, C.F. Woodward, Microstructure and room temperature properties of a high-entropy TaNbHfZrTi alloy, *J. Alloys Compd.* 509 (2011) 6043–6048.
- [13] W. Jiang, Y. Wang, X. Wang, B. Jiang, T. Ma, H. Kang, D. Zhu, Effect of Al on microstructure and mechanical properties of lightweight $\text{Al}_x\text{Nb}_{0.5}\text{TiV}_2\text{Zr}_{0.5}$ refractory high entropy alloys, *Mater. Sci. Eng., A* 865 (2023) 144628.
- [14] L. Li-Yan, C. Shu-nan, L. Yi, J. Gang, C. Hai-Dong, J. Yun-Jie, L. Chang-Jiu, L. Cheng-Xin, Microstructure and mechanical properties of lightweight $\text{Al}_x\text{CrNbTiV}$ ($x = 0.2, 0.5, 0.8$) refractory high entropy alloys, *Int. J. Refract. Hard Met.* 104 (2022) 105784.
- [15] B. Dou, Y. Pan, S. Liu, B. Wang, B. Cheng, L. Wang, S. Sun, Y. Xue, Achieving outstanding strength-ductility matching in BCC light-weight high entropy alloys via high content ordered nanoprecipitates, *Mater. Sci. Eng., A* 889 (2024) 145861.
- [16] Y. Chen, N. Li, Y. Wang, K. Liu, Y. Chang, M. Li, Phase evolution and mechanical properties of low-activation refractory high-entropy alloy $\text{Ti}_{1.5}\text{ZrV}_{0.5}\text{Ta}_{0.5}$, *J. Mater. Sci. Technol.* 174 (2024) 145–156.
- [17] I. Toda-Caraballo, A general formulation for solid solution hardening effect in multicomponent alloys, *Scripta Mater.* 127 (2017) 113–117.
- [18] I. Toda-Caraballo, P.E.J. Rivera-Díaz-del-Castillo, Modelling solid solution hardening in high entropy alloys, *Acta Mater.* 85 (2015) 14–23.
- [19] C. Lin, C. Juan, C. Chang, C. Tsai, J. Yeh, Effect of Al addition on mechanical properties and microstructure of refractory $\text{Al}_x\text{HfNbTaTiZr}$ alloys, *J. Alloys Compd.* 624 (2015) 100–107.
- [20] O.N. Senkov, S.V. Senkova, C. Woodward, Effect of aluminum on the microstructure and properties of two refractory high-entropy alloys, *Acta Mater.* 68 (2014) 214–228.
- [21] H. Wang, W. Chen, C. Chu, Z. Fu, Z. Jiang, X. Yang, E.J. Lavernia, Microstructural evolution and mechanical behavior of novel $\text{Ti}_{1.6}\text{ZrNbAl}$ lightweight refractory high-entropy alloys containing BCC/B2 phases, *Mater. Sci. Eng., A* 885 (2023) 145661.
- [22] S. Zeng, Y. Zhu, W. Li, H. Zhang, H. Zhang, Z. Zhu, A single-phase $\text{Ti}_{3}\text{Zr}_{1.5}\text{NbVAl}_{0.5}$ refractory high entropy alloy with excellent combination of strength and toughness, *Mater. Lett.* 323 (2022) 132548.
- [23] Y. Chen, Z. Xu, M. Wang, Y. Li, C. Wu, Y. Yang, A single-phase $\text{V}_{0.5}\text{Nb}_{0.5}\text{ZrTi}$ refractory high-entropy alloy with outstanding tensile properties, *Mater. Sci. Eng., A* 792 (2020) 139774.
- [24] B. Schuh, B. Völker, J. Todt, N. Schell, L. Perrière, J. Li, J.P. Couzinié, A. Hohenwarter, Thermodynamic instability of a nanocrystalline, single-phase TiZrNbHfTa alloy and its impact on the mechanical properties, *Acta Mater.* 142 (2018) 201–212.
- [25] Z. Lei, X. Liu, Y. Wu, H. Wang, S. Jiang, S. Wang, X. Hui, Y. Wu, B. Gault, P. Kontis, D. Raabe, L. Gu, Q. Zhang, H. Chen, H. Wang, J. Liu, K. An, Q. Zeng, T. Nieh, Z. Lu, Enhanced strength and ductility in a high-entropy alloy via ordered oxygen complexes, *Nature* 563 (2018) 546–550.
- [26] G. Dirras, L. Lilienstein, P. Djemja, M. Laurent-Brocq, D. Tingaud, J.P. Couzinié, L. Perrière, T. Chauveau, I. Guillot, Elastic and plastic properties of as-cast equimolar TiHfZrTaNb high-entropy alloy, *Mater. Sci. Eng., A* 654 (2016) 30–38.
- [27] S. Wang, S. Lu, M. Wu, D. Wang, G. Zhu, C. Yang, D. Shu, B. Sun, L. Vitos, Decreasing Zr content to improve tensile properties of non-equatomic TiZrHfNb medium entropy alloys with transformation-induced plasticity, *Mater. Sci. Eng., A* 832 (2022) 142476.
- [28] S. Wei, S.J. Kim, J. Kang, Y. Zhang, Y. Zhang, T. Furuhara, E.S. Park, C.C. Tasan, Natural-mixing guided design of refractory high-entropy alloys with as-cast tensile ductility, *Nat. Mater.* 19 (2020) 1175–1181.
- [29] S. Wang, E. Ma, J. Xu, New ternary equi-atomic refractory medium-entropy alloys with tensile ductility: Hafnium versus titanium into NbTa-based solution, *Intermetallics* 107 (2019) 15–23.
- [30] N. Yurchenko, E. Panina, A. Tojibaev, S. Zherebtsov, N. Stepanov, Overcoming the strength-ductility trade-off in refractory medium-entropy alloys via controlled B2 ordering, *Mater. Res. Lett.* 10 (2022) 813–823.
- [31] H. Huang, Y. Wu, J. He, H. Wang, X. Liu, K. An, W. Wu, Z. Lu, Phase-transformation ductilization of brittle high-entropy alloys via metastability engineering, *Adv. Mater.* 29 (2017) 1701678.
- [32] C. Juan, M. Tsai, C. Tsai, W. Hsu, C. Lin, S. Chen, S. Lin, J. Yeh, Simultaneously increasing the strength and ductility of a refractory high-entropy alloy via grain refining, *Mater. Lett.* 184 (2016) 200–203.
- [33] Y. Chen, Y. Li, X. Cheng, C. Wu, B. Cheng, Z. Xu, The microstructure and mechanical properties of refractory high-entropy alloys with high plasticity, *Materials* 11 (2018) 208.
- [34] X. Yan, P.K. Liaw, Y. Zhang, Ultrastrong and ductile BCC high-entropy alloys with low-density via dislocation regulation and nanoprecipitates, *J. Mater. Sci. Technol.* 110 (2022) 109–116.
- [35] S. Zherebtsov, N. Yurchenko, E. Panina, A. Tojibaev, M. Tikhonovsky, G. Salishchev, N. Stepanov, Microband-induced plasticity in a Ti-rich high-entropy alloy, *J. Alloys Compd.* 842 (2020) 155868.
- [36] Z. Guo, X. Shen, F. Liu, J. Guan, Y. Zhang, F. Dong, Y. Wang, X. Yuan, B. Wang, L. Luo, Y. Su, J. Cheng, Microstructure and mechanical properties of $\text{Al}_x(\text{TiZrTa}_{0.7}\text{NbMo})$ refractory high-entropy alloys, *J. Alloys Compd.* 960 (2023) 170739.
- [37] W. Xiong, A.X.Y. Guo, S. Zhan, C. Liu, S.C. Cao, Refractory high-entropy alloys: a focused review of preparation methods and properties, *J. Mater. Sci. Technol.* 142 (2023) 196–215.
- [38] J. Pang, H. Zhang, L. Zhang, Z. Zhu, H. Fu, H. Li, A. Wang, Z. Li, H. Zhang, A ductile $\text{Nb}_{40}\text{Ti}_{25}\text{Al}_{15}\text{V}_{10}\text{Ta}_5\text{Hf}_5\text{W}_2$ refractory high entropy alloy with high specific strength for high-temperature applications, *Mater. Sci. Eng., A* 831 (2022) 142290.
- [39] Z.Q. Xu, Z.L. Ma, M. Wang, Y.W. Chen, Y.D. Tan, X.W. Cheng, Design of novel low-density refractory high entropy alloys for high-temperature applications, *Mater. Sci. Eng., A* 755 (2019) 318–322.
- [40] J. Pang, H. Zhang, Y. Ji, Z. Zhu, L. Zhang, H. Li, A. Wang, H. Zhang, High-temperature structural and mechanical stability of refractory high-entropy alloy $\text{Nb}_{40}\text{Ti}_{25}\text{Al}_{15}\text{V}_{10}\text{Ta}_5\text{Hf}_5\text{W}_2$, *Mater. Charact.* 205 (2023) 113321.
- [41] Y. Chen, N. Li, Y. Wang, K. Liu, Y. Chang, M. Li, Phase evolution and mechanical properties of low-activation refractory high-entropy alloy $\text{Ti}_{1.5}\text{ZrV}_{0.5}\text{Ta}_{0.5}$, *J. Mater. Sci. Technol.* 174 (2024) 145–156.

- [42] O.N. Senkov, J.M. Scott, S.V. Senkova, F. Meisenkothen, D.B. Miracle, C. F. Woodward, Microstructure and elevated temperature properties of a refractory TaNbHfZrTi alloy, *J. Mater. Sci.* 47 (2012) 4062–4074.
- [43] T. Cao, W. Guo, W. Lu, Y. Xue, W. Lu, J. Su, C.H. Liebscher, C. Li, G. Dehm, Strain rate dependent deformation behavior of BCC-structured Ti₂₉Zr₂₄Nb₂₃Hf₂₄ high entropy alloy at elevated temperatures, *J. Alloys Compd.* 891 (2022) 161859.
- [44] S. Ozan, J. Lin, W. Weng, Y. Zhang, Y. Li, C. Wen, Effect of thermomechanical treatment on the mechanical and microstructural evolution of a β -type Ti-40.7Zr-24.8Nb alloy, *Bioact. Mater.* 4 (2019) 303–311.
- [45] W. Hsu, T. Shen, Y. Liang, J. Yeh, C. Tsai, In situ analysis of the Portevin-Le Chatelier effect from low to high-entropy alloy in equal HfNbTaTiZr system, *Acta Mater.* 253 (2023) 118981.
- [46] X. Zeng, F. Li, X. Zhou, W. Yan, J. Li, D. Yang, Q. Shen, X. Wang, M. Liu, The phase stability at intermediate-temperature and mechanical behavior of the dual-phase AlCoCr_{0.5}Fe₃Ni_{2.5} high entropy alloys, *Mater. Chem. Phys.* 297 (2023) 127314.
- [47] X. Yang, Y. Zhang, Prediction of high-entropy stabilized solid-solution in multi-component alloys, *Mater. Chem. Phys.* 132 (2012) 233–238.
- [48] A. Takeuchi, A. Inoue, Classification of bulk metallic glasses by atomic size difference, heat of mixing and period of constituent elements and its application to characterization of the main alloying element, *Mater. Trans.* 46 (2005) 2817–2829.
- [49] H. Zhang, N. Gao, W. Bai, M. Rong, J. Wang, L. Zhang, L. Liu, Diffusivities and atomic mobilities in bcc Ti-V-Mo alloys, *Calphad* 83 (2023) 102633.
- [50] J.O. Andersson, T. Helander, L. Höglund, P. Shi, B. Sundman, Thermo-Calc and DICTRA, computational tools for materials science, *Calphad* 26 (2002) 273–312.
- [51] S. Chen, K. Tseng, Y. Tong, W. Li, C. Tsai, J. Yeh, P.K. Liaw, Grain growth and Hall-Petch relationship in a refractory HfNbTaZrTi high-entropy alloy, *J. Alloys Compd.* 795 (2019) 19–26.
- [52] S. Zherebtsov, N. Yurchenko, E. Panina, M. Tikhonovsky, N. Stepanov, Gum-like mechanical behavior of a partially ordered Al₅Nb₂₄Ti₄₀V₅Zr₂₆ high entropy alloy, *Intermetallics* 116 (2020) 106652.
- [53] S. Wang, J. Xu, (TiZrNbTa)-Mo high-entropy alloys: dependence of microstructure and mechanical properties on Mo concentration and modeling of solid solution strengthening, *Intermetallics* 95 (2018) 59–72.
- [54] H.W. Yao, J.W. Qiao, J.A. Hawk, H.F. Zhou, M.W. Chen, M.C. Gao, Mechanical properties of refractory high-entropy alloys: experiments and modeling, *J. Alloys Compd.* 696 (2017) 1139–1150.
- [55] Y. Cao, W. Zhang, B. Liu, Y. Liu, M. Du, A. Fu, Phase decomposition behavior and its effects on mechanical properties of TiNbTa_{0.5}ZrAl_{0.5} refractory high entropy alloy, *J. Mater. Sci. Technol.* 66 (2021) 10–20.